molecules

MDPI

Article

Isotopic Transient Kinetic Analysis of Soot Oxidation on Mn_3O_4, Mn_3O_4-CeO_2, and CeO_2 Catalysts in Tight Contact Conditions

Marek Rotko * and Karolina Karpińska-Wlizło

Department of Chemical Technology, Institute of Chemical Sciences, Faculty of Chemistry, Maria Curie-Skłodowska University, 3 Maria Curie-Skłodowska Square, 20-031 Lublin, Poland
* Correspondence: marek.rotko@mail.umcs.pl

Abstract: The reaction mechanism of soot oxidation on Mn (Mn_3O_4), Mn-Ce (Mn_3O_4-CeO_2), and Ce (CeO_2) catalysts in tight contact conditions was investigated using ITKA (isotopic transient kinetic analysis). The obtained results suggest that lattice-bulk oxygen from all studied catalysts takes part in the soot oxidation process but with varying relative contributions: for the Ce catalyst, this contribution is practically 100%, whereas with decreasing Ce content in Mn-Ce catalysts, the significance of lattice-bulk oxygen for soot oxidation diminishes. For the Mn catalyst, it is estimated to be below 50%. Moreover, strong interactions between Mn and Ce ions were observed, increasing oxygen mobility in the catalyst crystal lattice and affecting the activity of Mn-Ce catalysts.

Keywords: diesel soot oxidation; CeO_2; Mn_3O_4; Mn_3O_4-CeO_2; ITKA

1. Introduction

The catalyzed diesel particulate filter (CDPF) is a crucial element of diesel exhaust purification technology aimed at reducing emissions of pollutants [1,2]. Catalytic substances enable passive regeneration of the DPF filter—the deposited soot is burned without requiring fuel to be added or heating. However, the main components of the catalytically active substances used in the CDPF filter are noble metals, in particular, platinum, which demonstrate very high catalytic activity [3–5]. To reduce the dependence on rare and expensive precious metals, other catalytic materials are being sought. Cerium oxide is one of the potential alternatives. Numerous studies [6–10] have shown its high activity in soot oxidation and its good stability. Cerium oxide can easily change its oxidation state between Ce^{3+} and Ce^{4+}, which gives it an excellent ability to store and relieve high amounts of oxygen, depending on the atmosphere—oxidizing or reducing. Moreover, its catalytic properties in soot oxidation can be improved by adding a small number of various modifiers [11–14] or mixing with a large amount of various catalytically active phases of soot oxidation [15–20]. In this context, the modification of CeO_2 through the addition of manganese oxides or mixing with them deserves special attention. Manganese oxides are among the common transition metal oxides, offering advantages such as low cost, environmental friendliness, and unique redox properties associated with their easily achievable variable valence states (Mn^{2+}, Mn^{3+}, and Mn^{4+}). Manganese oxides demonstrate a good ability to remove soot from the DPF surface [21–27], especially in the presence of nitrogen oxides, because they are characterized by high catalytic activity in NO oxidation to NO_2. NO_2 is a well-known stronger oxidant than molecular oxygen, and technology

check for updates

Academic Editor: Shaojun Yuan

Received: 26 November 2024
Revised: 3 January 2025
Accepted: 14 January 2025
Published: 16 January 2025

Citation: Rotko, M.; Karpińska-Wlizło, K. Isotopic Transient Kinetic Analysis of Soot Oxidation on Mn_3O_4, Mn_3O_4-CeO_2, and CeO_2 Catalysts in Tight Contact Conditions. *Molecules* **2025**, *30*, 343. https://doi.org/10.3390/molecules30020343

Copyright: © 2025 by the authors. Licensee MDPI, Basel, Switzerland. This article is an open access article distributed under the terms and conditions of the Creative Commons Attribution (CC BY) license (https://creativecommons.org/licenses/by/4.0/).

based on this compound is commercially used to purify exhaust gases from diesel vehicles that use platinum catalysts.

In the case of the process of soot oxidation on pure cerium oxide and in tight contact conditions, it seems that the main role is played by oxygen stored inside of the crystal lattice—the Mars–van Krevelen reaction mechanism [28–30]. However, some researchers [31,32] propose a spillover mechanism, where the main role is played by reactive oxygen species (peroxide and superoxide ions) formed on the catalyst surface. The addition of modifiers can loosen the bonds in the crystal lattice and facilitate the migration of oxygen, but it can also cause a change in the reaction mechanism or the appearance of an alternative reaction pathway, which has been observed in previous studies [30] for the Co_3O_4-CeO_2 catalyst.

According to results obtained by Wagloehner et al. [21], the reaction mechanism of soot oxidation on Mn_3O_4 and in tight contact conditions is similar to that observed for CeO_2—soot is mainly oxidized by oxygen from the crystal lattice of Mn_3O_4. The authors estimated that the participation of bulk oxygen in soot oxidation reaches approximately 60%. It is difficult to find studies in the literature investigating the reaction mechanism of soot oxidation on pure or nearly pure Mn_3O_4 under tight contact conditions and in the absence of NO.

The process of soot oxidation on Mn_3O_4-CeO_2 in tight contact conditions and without NO has only been studied by a few scientists [19,20]. Jampaiah et al. [19] tested catalysts with various amounts (10% to 40%) of Mn_3O_4 loading on CeO_2. The highest activity was demonstrated by the catalyst containing 20% Mn_3O_4, and the rise in catalytic ability was assigned to the increase in redox properties. However, this study [19], as well as our previous study [20], does not supply information about the reaction mechanism. Studies on the reaction mechanism of soot oxidation on pure or nearly pure Mn_3O_4 under tight contact conditions and without NO are scarce in the literature. Moreover, the mechanism of soot oxidation has also been analyzed in the case of pure CeO_2 and Mn_3O_4. For mechanistic studies and oxygen mobility under soot oxidation process conditions, isotopic transient kinetic analysis (ITKA) was used. The ITKA experiments were conducted according to the conditions and procedures described for steady-state isotopic transient kinetic analysis [33–36], with the soot content decreasing over time, which reduced the concentration of the product (carbon dioxide) during the experiment.

2. Results and Discussion

2.1. Catalysts' Physicochemical Properties

The chemical composition of the prepared catalysts is presented in Table 1. The XRF results demonstrate that the obtained values of the manganese-to-cerium molar ratio are almost identical to those planned during preparation.

Table 1. Metal content in manganese, manganese–cerium, and cerium catalysts determined via XRF.

Catalyst	Metal Content (% wt.)		Molar Ratio (Mn:Ce)
	Mn	Ce	
Mn	71.0	0.0	1.00:0.00
0.75Mn-0.25Ce	40.2	31.7	0.76:0.24
0.5Mn-0.5Ce	22.6	53.1	0.52:0.48
0.25Mn-0.75Ce	9.6	70.6	0.26:0.74
Ce	0.0	81.2	0.00:1.00

The results of the nitrogen adsorption/desorption experiment show that the BET surface area for manganese–cerium catalysts is more than 10 times larger compared to

the manganese catalyst and close to the surface area of the cerium catalyst (Table 2). On the other hand, the average pore diameter for the manganese catalyst is several times larger, while the volume of pores is comparable to the cerium catalyst but lower than the manganese–cerium catalysts.

Table 2. Total BET surface area, average pore diameter, and volume of pores determined for manganese, manganese–cerium, and cerium catalysts.

Catalyst	Total BET Surface Area (m^2/g)	Average Pore Diameter (nm)	Volume of Pores (cm^3/g)
Mn	7.5	30.94	0.05
0.75Mn-0.25Ce	76.5	7.77	0.14
0.5Mn-0.5Ce	101.6	5.81	0.10
0.25Mn-0.75Ce	102.0	6.11	0.07
Ce	85.9	5.51	0.04

The crystal structure of the tested catalysts consists mainly of Mn_3O_4 and CeO_2 (Table 3 and Figure S1). A small amount (about 5%) of Mn_2O_3 was also detected for the manganese catalyst. In the manganese–cerium catalytic systems, the crystallite size of the Mn_3O_4 phase is much smaller (2–9 times) than in the pure manganese catalyst. In contrast, the size of CeO_2 crystallites is comparable to the crystallite size in the pure cerium catalyst.

Table 3. Phase composition and crystallite size obtained via XRD for manganese, manganese–cerium, and cerium catalysts.

Catalyst	Crystallographic Phases			Mean Size of Crystallites (nm)
	Chemical Formula	Content (%)	Crystallite Size (nm)	
Mn	Mn_3O_4 Mn_2O_3	95 5	70.8 49.8	69.7
0.75Mn-0.25Ce	Mn_3O_4 CeO_2	34 66	29.8 17.8	21.9
0.5Mn-0.5Ce	Mn_3O_4 CeO_2	8 92	18.3 10.9	11.5
0.25Mn-0.75Ce	Mn_3O_4 CeO_2	2 98	7.2 13.3	13.1
Ce	CeO_2	100	16.4	16.4

The composition of the crystal structure of the catalysts was also studied using Raman spectroscopy (Figure 1). The intense band at 464 cm^{-1} is attributed to the F_{2g} vibrational mode of the cubic structure of CeO_2 [37–44], while the second intense band at 657 cm^{-1} is assigned to the A_{1g} vibrational mode of the spinel structure of Mn_3O_4 [38–41,44–47]. Moreover, in the case of the pure Mn catalyst, the presence of the Mn_3O_4 phase is also indicated by the small bands at 288, 317, and 374 cm^{-1}. On the other hand, the feeble signal observed for Mn-Ce catalysts may suggest well-mixed components, strong interaction between CeO_2 and Mn_3O_4, and deformation of their structure.

The XPS results (Figure 2a,b) show that the surface of the studied catalysts consists of Mn_3O_4 [19,38–40,42,43,45,47–50] and CeO_2 [19,38–40,42,43,45,48–50]. The detailed analysis of the $3d_{3/2}$ and $3d_{5/2}$ spectra shows that the content of Ce^{3+} ions (Table S1) is not high and does not exceed 10%.

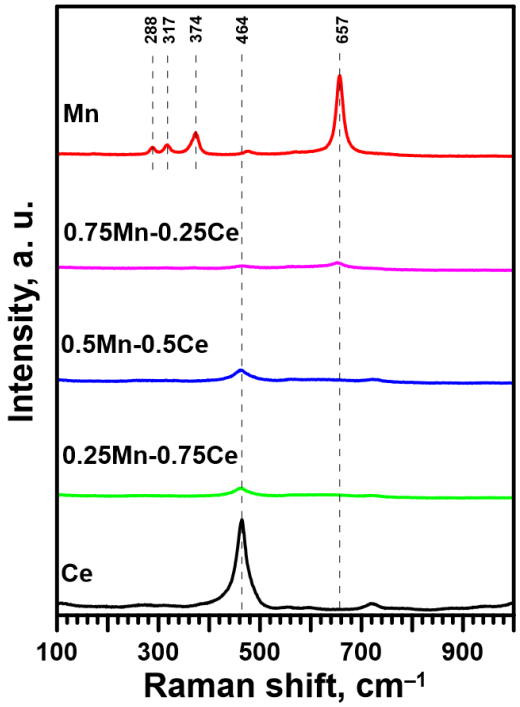


Figure 1. Raman spectra for Mn, Mn-Ce, and Ce catalysts.

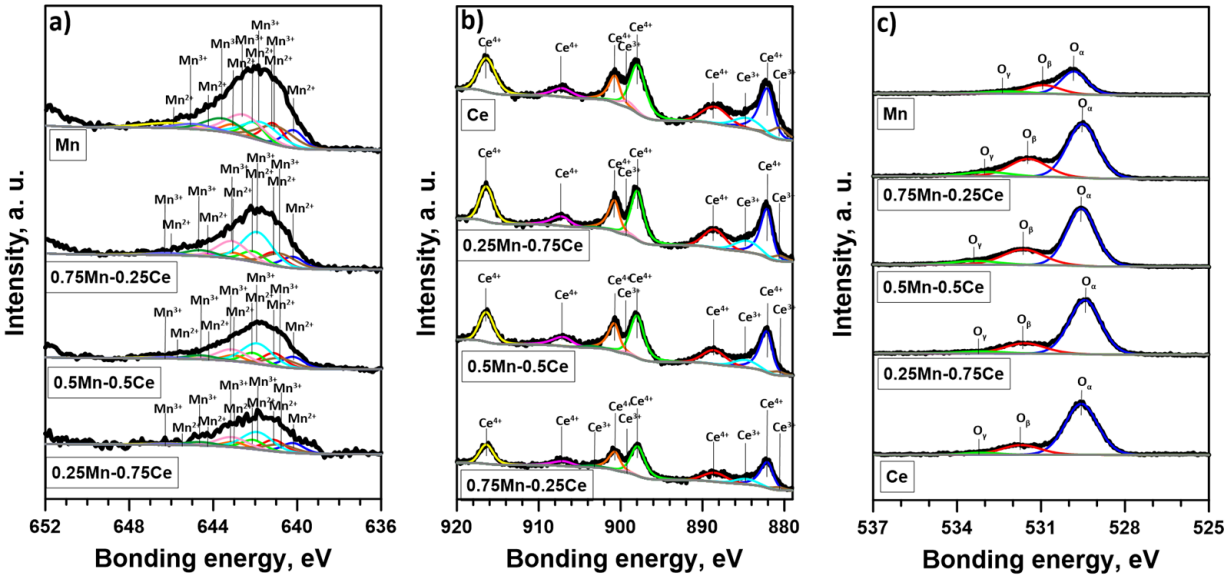


Figure 2. High-resolution XPS spectra of Mn $2p_{3/2}$ (**a**), Ce $3d_{3/2}$ and Ce $3d_{5/2}$ (**b**), and O 1s (**c**) obtained for the tested catalysts.

Moreover, the analysis of O 1s spectra suggests that different oxygen species are present on the surface of the tested catalysts (Figure 2c and Table S1). The maximum of the signal at about 529 eV (O_α) is attributed to lattice oxygen, while the maxima of the signal at about 531 eV (O_β) and about 533 eV (O_γ), according to the literature [19,38–40,42,43,45,48,49], correspond to various forms of absorbed oxygen (carbonates, hydroxyl groups, etc.) but can also be assigned to defects in the oxide structure.

2.2. Catalytic Performance

The mixed oxides demonstrate higher catalytic activity than the pure ones (Figures 3 and S2). The best is the 0.25Mn-0.75Ce catalyst, followed by 0.5Mn-0.5Ce

and 0.75Mn-0.25Ce. On the other hand, the worst is the Mn catalyst, followed by Ce. The difference between the most active 0.25Mn-0.75Ce catalyst and the worst is about 50 °C. All catalysts start oxidizing soot within a temperature range of 250–320 °C, while complete soot conversion is observed at around 450–500 °C.

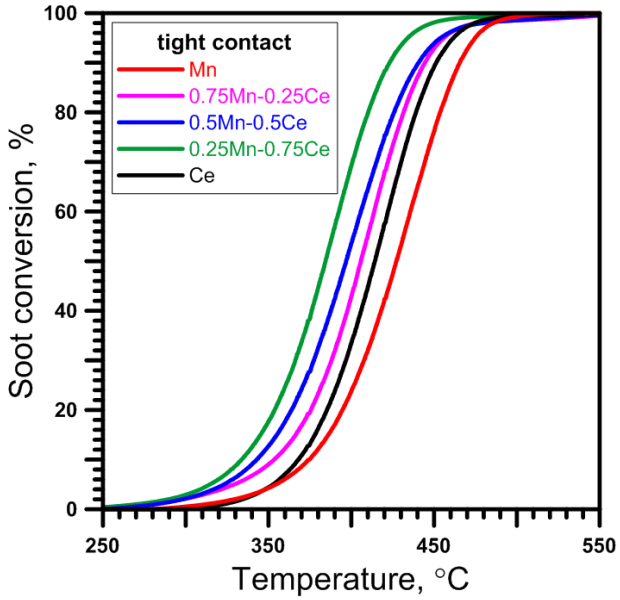


Figure 3. Activity of Mn, Mn-Ce, and Ce catalysts in soot oxidation under tight contact conditions.

A similar result was observed by Jampaiah et al. [19] in their study of catalysts containing varying amounts of Mn_3O_4 (from 10% to 40%) on CeO_2, where the catalyst with 20% Mn_3O_4 showed the best performance. The high activity of this catalyst was explained by its optimal redox properties. Moreover, in the literature [51] a comparable effect can be found, among others, for Co_3O_4-CeO_2 catalysts.

Besides the chemical composition, the most active catalyst (0.25Mn-0.75Ce) has similar physicochemical properties to other Mn-Ce catalysts: the bulk (Table 3 and Figure 1) and surface (Figure 2) phase composition is practically the same; the total BET surface area (Table 2) is comparable to that of the 0.5Mn-0.5Ce catalyst but slightly larger than that of the 0.75Mn-0.25Ce catalyst; and the greatest differences can be observed in the size of crystallites (Table 3). For the 0.25Mn-0.75Ce catalyst, the size of Mn_3O_4 crystallites is more than twice as small as that of the 0.5Mn-0.5Ce catalyst and four times smaller than that of the 0.75Mn-0.25Ce catalyst. However, caution should be exercised when considering the influence of Mn_3O_4 crystal size on catalytic activity, as the observed reflection intensity (Figure S1) for the Mn_3O_4 phase was very low. On the other hand, the size of the CeO_2 crystallites of the 0.25Mn-0.75Ce catalyst (13.3 nm) is slightly larger than the 0.5Mn-0.5Ce catalyst (10.9 nm) and slightly smaller than the 0.75Mn-0.25Ce catalyst (17.8 nm).

2.3. Oxidizability and Reducibility of the Catalytic Phase

Since the calculations (Table S1) resulting from the XPS results suggest differences in the number of oxygen vacancies and the amount of adsorbed oxygen on the surface of the Mn-Ce catalysts, their reduction and oxidation capabilities were also tested. The TPR results (Figure 4a and Table S2) show that the Mn-Ce catalysts reduce at a lower temperature than the Mn catalyst. Furthermore, the Mn_3O_4 reduction steps are separated in the case of Mn-Ce catalysts. According to the literature [19,52], the first peak can be ascribed to the reduction of Mn^{3+} ions in the tetrahedral position to Mn^{2+}, while the second is related to the reduction of the remaining Mn^{3+} ions to Mn^{2+}. However, no significant variations in the reduction temperature were observed between the Mn-Ce catalysts, except

for those due to the Mn content, with only a slight shift of the reduction maxima towards lower temperatures for the 0.25Mn-0.75Ce catalyst. CeO_2 starts to reduce (Ce^{4+} to Ce^{3+}) at temperatures above 600 °C, while the observed small peak at about 500 °C is related, according to the literature [45], to the removal of oxygen-adsorbed species. However, the TPO results (Figure 4b) suggest that the CeO_2 reduction peak at about 500 °C can also be assigned to a partial reduction of its surface. This argument can be supported by the fact that the TPO results were obtained after the pre-reduction of the catalyst samples at 600 °C.

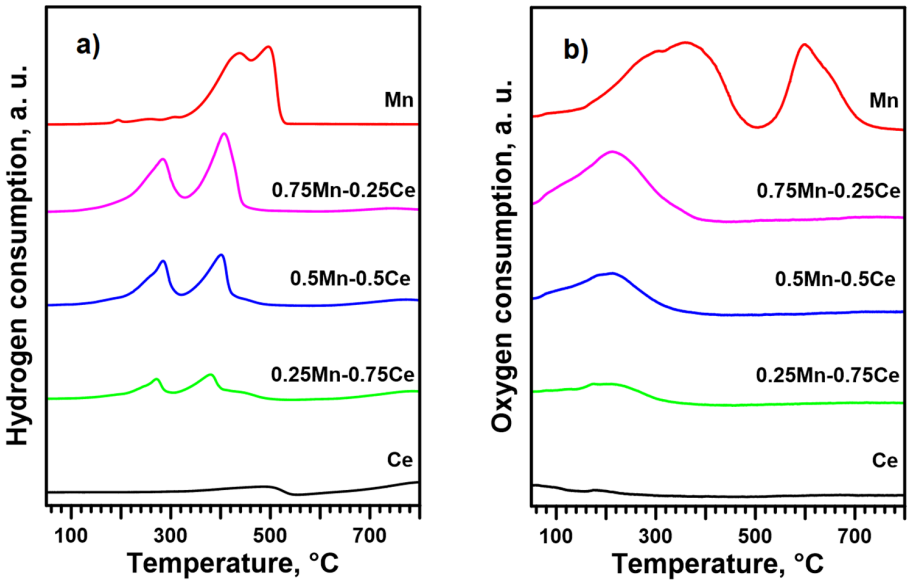


Figure 4. TPR (**a**) and TPO (**b**) results for the analyzed catalysts.

The TPO results (Figure 4b) show that the Mn-Ce catalysts are re-oxidized extremely easily compared to the Mn catalyst. This means that oxygen (removed during reduction at 500 °C) in the crystal lattice of the Mn-Ce catalysts can be almost completely replenished at temperatures below the temperatures of soot oxidation (Figure 3). However, one should be aware that the structure/composition of the recreated manganese oxide phase during this experiment may be completely different from the original one. Regardless, assuming that there are no structure/composition differences between the Mn-Ce catalysts, it can be stated that their various activities remain unexplained, as no shifts between the re-oxidation temperatures are seen.

2.4. Oxygen Mobility

The ITKA results (Figures 5a–9a) show that oxygen from the catalyst lattice of Mn and Ce catalysts does not exchange with oxygen from the gas phase, whereas oxygen from the lattice of Mn-Ce catalysts does during soot oxidation. The number of exchanged oxygen molecules increases with increasing Mn content in the Mn-Ce catalysts. In the case of the 0.25Mn-0.75Ce catalyst, only a small amount of oxygen (Figure 8a) is involved in the exchange process, whereas for the 0.5Mn-0.5Ce (Figure 7a) and 0.75Mn-0.25Ce (Figure 6a) catalysts, these amounts are much more visible. This means that the mobility of oxygen increases with increasing Mn content in the Mn-Ce catalysts. The results suggest that oxygen exchange between the gas phase and the catalyst crystal lattice occurs independently of the soot oxidation process, as oxygen mobility changes in the opposite direction to the activity of the tested Mn-Ce catalysts. Moreover, it can also be suggested that the too-high oxygen mobility in the crystal lattice of the catalysts may not favor their catalytic abilities.

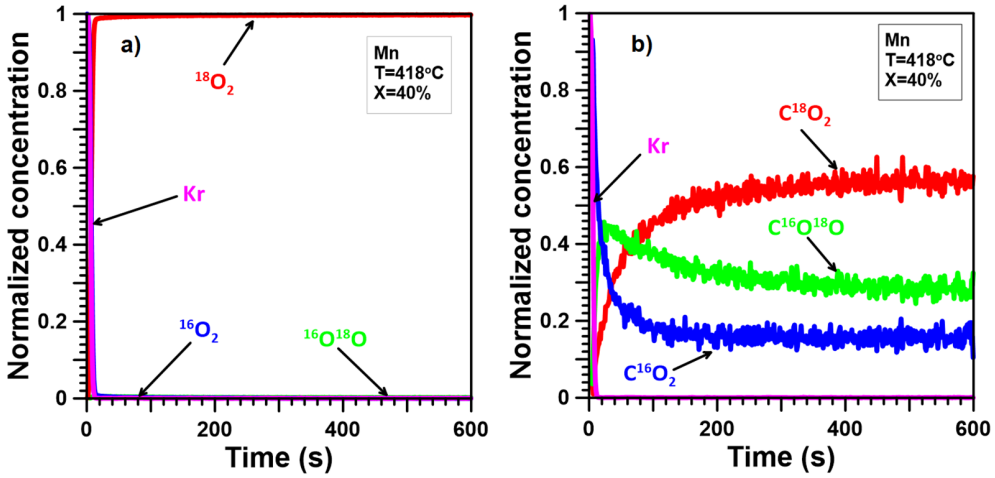


Figure 5. ITKA results obtained for the Mn catalyst at the temperature corresponding to 40% soot conversion ((**a**)—changes in $^{16}O_2$, $^{16}O^{18}O$, and $^{18}O_2$ concentration; (**b**)—changes in $C^{16}O_2$, $C^{16}O^{18}O$, and $C^{18}O_2$ concentration observed after switching from $^{16}O_2$/Kr/Ar/He to $^{18}O_2$/Ar/He).

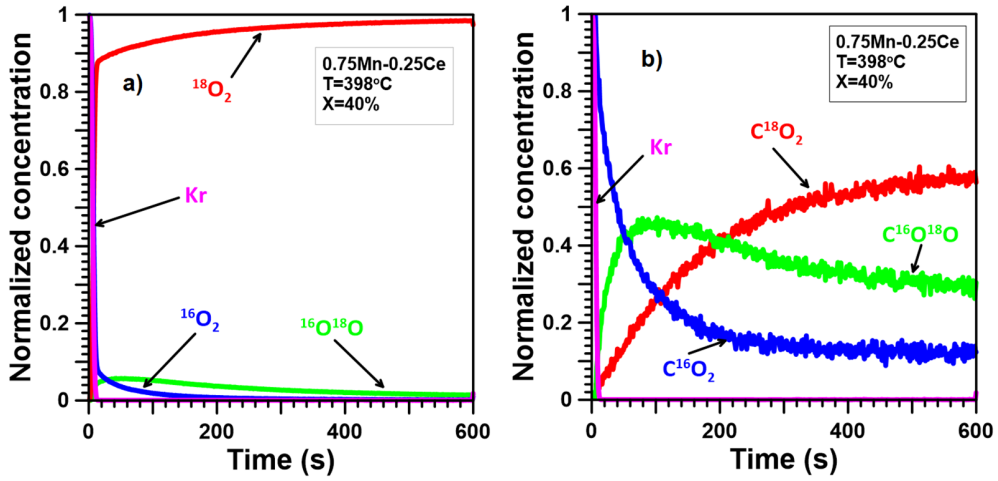


Figure 6. ITKA results obtained for the 0.75Mn-0.25Ce catalyst at the temperature corresponding to 40% soot conversion ((**a**)—changes in $^{16}O_2$, $^{16}O^{18}O$, and $^{18}O_2$ concentration; (**b**)—changes in $C^{16}O_2$, $C^{16}O^{18}O$, and $C^{18}O_2$ concentration observed after switching from $^{16}O_2$/Kr/Ar/He to $^{18}O_2$/Ar/He).

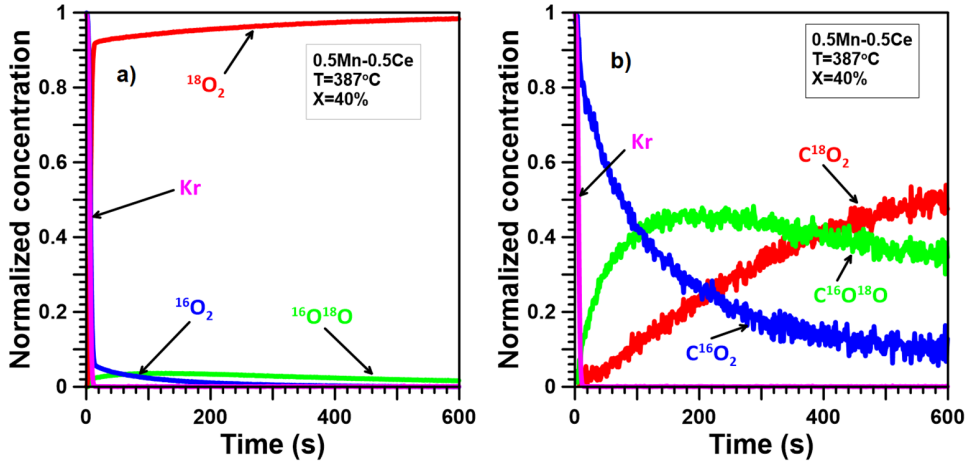


Figure 7. ITKA results obtained for the 0.5Mn-0.5Ce catalyst at the temperature corresponding to 40% soot conversion ((**a**)—changes in $^{16}O_2$, $^{16}O^{18}O$, and $^{18}O_2$ concentration; (**b**)—changes in $C^{16}O_2$, $C^{16}O^{18}O$, and $C^{18}O_2$ concentration observed after switching from $^{16}O_2$/Kr/Ar/He to $^{18}O_2$/Ar/He).

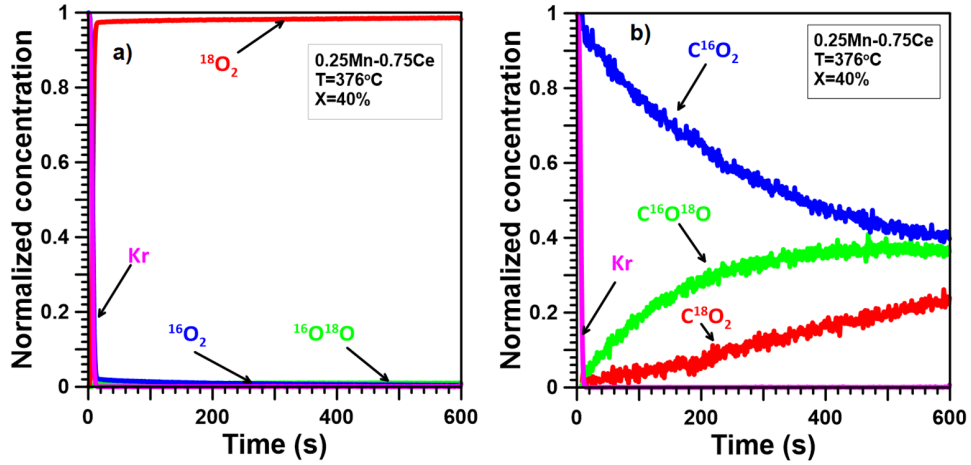


Figure 8. ITKA results obtained for the 0.25Mn-0.75Ce catalyst at the temperature corresponding to 40% soot conversion ((**a**)—changes in $^{16}O_2$, $^{16}O^{18}O$, and $^{18}O_2$ concentration; (**b**)—changes in $C^{16}O_2$, $C^{16}O^{18}O$, and $C^{18}O_2$ concentration observed after switching from $^{16}O_2$/Kr/Ar/He to $^{18}O_2$/Ar/He).

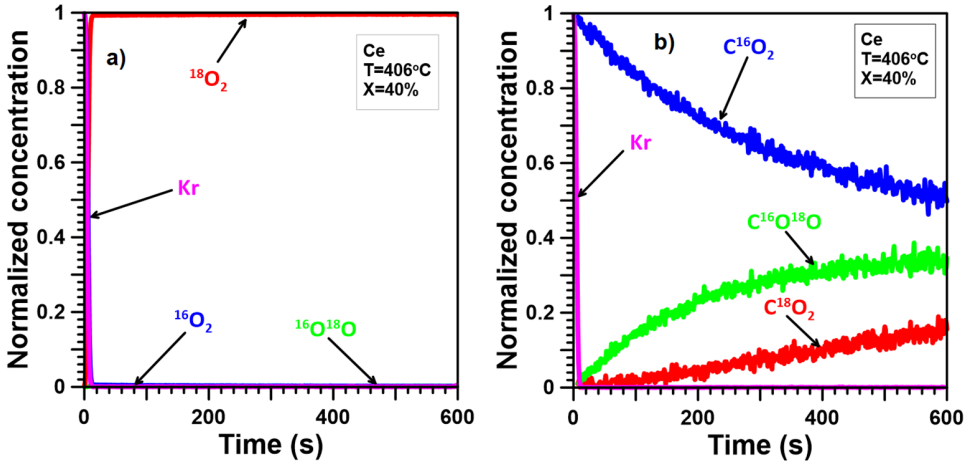


Figure 9. ITKA results obtained for the Ce catalyst at the temperature corresponding to 40% soot conversion ((**a**)—changes in $^{16}O_2$, $^{16}O^{18}O$, and $^{18}O_2$ concentration; (**b**)—changes in $C^{16}O_2$, $C^{16}O^{18}O$, and $C^{18}O_2$ concentration observed after switching from $^{16}O_2$/Kr/Ar/He to $^{18}O_2$/Ar/He).

2.5. Reaction Mechanism

The ITKA results (Figures 5b–9b) show that oxygen originating from the crystal lattice of Mn, Mn-Ce, and Ce catalysts takes part in the oxidation of soot. Nevertheless, the contribution of lattice-bulk oxygen to soot oxidation varies and increases with increasing Ce content in Mn-Ce catalysts. In the case of the Mn catalyst (Figure 5b), the concentration of $C^{16}O_2$ drops to about 20% within 100–150 s. After this time, the rate of $C^{16}O_2$ decline slows down drastically. At the same time, the $C^{18}O_2$ signal demonstrates similar but opposite changes. The $C^{16}O^{18}O$ signal initially increases at a high rate, reaching a maximum after 10–20 s, and later, its values decline to a more or less stable position. The $C^{16}O_2$, $C^{16}O^{18}O$, and $C^{18}O_2$ signals demonstrate this after switching between isotopic mixtures, the concentration of CO_2 with the old oxygen atom(s) (^{16}O) decreases to approximately 40%. The behavior of the $C^{18}O_2$ signal just after isotopic switching indicates that soot is oxidized parallelly by oxygen from the crystal lattice bulk of the Mn catalyst and by surface oxygen. This means that the soot oxidation process takes place according to two competing/parallel reaction pathways/mechanisms: the first one is the classical redox mechanism (with lattice-bulk oxygen), while the second one is related to the oxidation of soot with oxygen chemically adsorbed on the catalyst surface and/or lattice oxygen only from the surface. These conclusions are consistent with the results obtained by Wagloehner

et al. [21], which suggest that the participation of bulk oxygen in soot oxidation reaches approximately 60%. Moreover, the obtained results for the Mn catalyst are very similar to our previous results [30] obtained for Co_3O_4. However, pure Co_3O_4 demonstrates slightly lower participation of bulk oxygen in soot oxidation than Mn_3O_4.

In the case of the Ce catalyst, the ITKA results (Figure 9b) are almost identical to those for the CeO_2 catalyst studied in our previous paper [30]. These results suggest the Mars–van Krevelen reaction mechanism because the observed $C^{18}O_2$ signal after the isotopic switch increases very slowly (after 50 s or even 100 s, it is still practically invisible). Similar behavior can be observed for the $C^{16}O^{18}O$ signal—it also slowly increases, while the $C^{16}O_2$ signal slowly decreases. Of course, these results cannot completely exclude the participation of chemisorbed oxygen and/or lattice oxygen only from the surface in the soot oxidation process, but its influence may only be very small.

In the case of the Mn-Ce catalysts, the observed (Figures 6b–8b) delays between the $C^{16}O_2$ curve and the Kr curve are smaller than for the Ce catalyst but still larger than for the Mn catalyst. Furthermore, the growth of the $C^{18}O_2$ concentration is quicker compared to the Ce catalyst and slightly gentler than for the Mn catalyst. The signal of $C^{16}O^{18}O$ grows much faster than for the Ce catalyst but still slower than for the Mn catalyst. This means that the mechanism of soot oxidation on the surface of the Mn-Ce catalysts differs slightly from those observed on the surface of pure CeO_2 and Mn_3O_4. However, it can generally be stated that the reaction mechanism proposed for Mn-Ce catalysts must partially contain elements characteristic of both CeO_2 and Mn_3O_4 since the observed shape of the $C^{16}O_2$, $C^{16}O^{18}O$, and $C^{18}O_2$ signals is intermediate/between the signals typical of CeO_2 and Mn_3O_4. Additionally, the $C^{16}O_2$, $C^{16}O^{18}O$, and $C^{18}O_2$ signals observed for Mn-Ce catalysts depend on the element content. Increasing the Ce content in Mn-Ce catalysts causes a larger number of oxygen atoms from the deeper layers of the catalyst lattice to participate in soot oxidation. In the case of the 0.25Mn-0.75Ce, the process of soot oxidation proceeds according to the Mars–van Krevelen mechanism, similar to pure CeO_2, and the probability of soot oxidation according to the alternative mechanism(s) can be limited to a few percent. On the other hand, both 0.75Mn-0.25Ce and 0.5Mn-0.5Ce catalysts demonstrate a much greater impact of chemisorbed oxygen and/or lattice oxygen only from the surface on the process of soot oxidation, making their behavior closer to that of pure Mn_3O_4.

Summing up this part, it can be stated that the interaction between CeO_2 and Mn_3O_4 increases the catalyst redox properties of catalysts (accelerating the transfer of oxygen within the crystal lattice), and consequently, the Mn-Ce catalysts are more active than pure CeO_2. However, as the amount of Mn_3O_4 increases, the number of active centers generated by CeO_2 decreases, resulting in the lower activity of 0.75Mn-0.25Ce and 0.5Mn-0.5Ce than 0.25Mn-0.75Ce.

3. Materials and Methods

3.1. Catalyst Preparation

Catalytic materials were prepared with the co-precipitation method using aqueous solutions of cerium and manganese acetate (Sigma-Aldrich, Burlington, MA, USA). Synthesis was carried out in a jacketed reactor (Radleys, Saffron Walden, UK) at 60 °C by dosing (5 cm^3/min) the precipitation agent (ammonium carbonate) with a peristaltic pump until pH = 7.8. The obtained suspension was stirred using a mechanical mixer at 300 rpm. After two hours of conditioning, the precipitate was filtered off, washed with deionized water to pH = 7, and pre-dried with anhydrous alcohol. The filtration, washing, and pre-drying operations were carried out using a centrifuge. The catalyst precursors were dried at 110 °C and calcinated at 500 °C for 2 h. For testing in the catalytic reactor (activity and ITKA measurements), the catalyst samples were mixed with soot (Printex U, Evonik Industries,

Essen, Germany), pressed, and then ground to a fraction of 0.15–0.3 mm to obtain a tight contact mixture.

3.2. Physicochemical Characteristics

The metal content (Mn and Ce) of the tested catalytic materials was obtained via X-ray fluorescence (XRF). The total BET surface area, average pore size, and volume of pores were calculated from the physical nitrogen adsorption/desorption results. Using the XRD (X-ray diffraction) method, the type and share of crystallographic phases and the mean size of their crystallites were determined—more details are available in a previous publication [37].

The solid-phase composition of the tested catalytic materials was also analyzed via Raman spectroscopy using an inVia Reflex Renishaw spectrometer (Renishaw plc, Wotton-under-Edge, UK). The spectra were collected in the range from 100 cm^{-1} to 1000 cm^{-1} with a resolution of 1 cm^{-1}, after exposure to a 785 nm laser.

The surface of the tested catalytic materials was examined via X-ray photoelectron spectroscopy (XPS). For these purposes, a Prevac system (Rogów, Poland) with a monochromatic Al Kα source and a hemispherical electron analyzer, both manufactured by VG Scienta (Hastings, UK), was used. The studies were performed at an analyzer energy of 200 eV and an energy step of 0.5 eV and 0.1 eV for survey scan and high-resolution spectra, respectively.

3.3. Catalytic Studies

The activity of the catalytic materials was examined in the Microactivity Reference system from PID Eng& Tech (Madrid, Spain). The catalyst samples during the activity test contained 50 mg of the catalyst–soot mixture diluted with 450 mg of sand. The reaction mixture stream fed to the reactor at a rate of 100 cm^3/min consisted of 10 vol.% of oxygen, 10 vol.% of argon (internal standard), and helium as balance gas. The gas composition of the post-reaction mixture at the outlet of the fixed-bed quartz reactor was analyzed using an HPR 20 R&D quadrupole mass spectrometer from Hiden Analytical (Warrington, UK). With the progression of the analysis, the temperature of the catalytic reactor was increased linearly at the rate of 5 °C/min until all amounts of soot were oxidized.

3.4. Temperature-Programmed Reduction/Oxidation

Temperature-programmed reduction (TPR) and oxidation (TPO) were performed in an AutoChem II 2920 system (Micromeritics, Norcross, GA, USA) by heating the catalyst samples from 45 °C to 900 °C with a ramp of 10 °C/min. First, 50 mg of catalyst samples and mixtures of 5% O_2 in He and 5% H_2 in Ar fed at the rate of 30 cm^3/min were used. Before the TPR experiment, the catalytic samples were heated in O_2/He to the calcination temperature, while before the TPO experiment, the catalytic samples were reduced in H_2/Ar at 600 °C for 2 h.

3.5. Isotopic Transient Kinetic Analysis

The ITKA experiments were conducted in an apparatus similar to that used for the activity studies. Moreover, the composition of the catalyst bed and the total volumetric flow rate of the reaction mixture were the same. The reaction mixture had a slightly different composition and contained 10 vol.% of oxygen ($^{16}O_2$ or $^{18}O_2$), 10 vol.% of krypton (inert tracer), 10 vol.% of argon (internal standard), and helium as balance gas. The switching between $^{16}O_2$/Kr/Ar/He and $^{18}O_2$/Ar/He took place at a temperature corresponding to 40% soot conversion and after 10 min under isothermal conditions.

4. Conclusions

The results of our catalytic research confirm that the Mn-Ce catalysts (Mn_3O_4-CeO_2) demonstrate higher activity than pure oxides (Mn_3O_4 and CeO_2) in soot oxidation under tight contact conditions. Moreover, the activity of Mn-Ce catalysts can be arranged in the following sequence: 0.25Mn-0.75Ce > 0.5Mn-0.5Ce > 0.75Mn-0.25Ce. The most active catalyst (0.25Mn-0.75Ce) has, among others, the largest total surface area and the smallest Mn_3O_4 crystallite size and shows the lowest oxygen mobility. However, the reaction mechanism of soot oxidation on the 0.25Mn-0.75Ce catalyst is the strongest, similar to the pure CeO_2. The main amount (practically all) of soot is oxidized using oxygen from the catalyst crystal lattice bulk (Mars–van Krevelen mechanism). In the case of the remaining Mn-Ce catalysts (0.5Mn-0.5Ce and 0.75Mn-0.25Ce), the impact of chemisorbed oxygen and/or lattice oxygen only from the surface on soot oxidation is higher and increases with increasing Mn_3O_4 content. The obtained results for pure Mn_3O_4 indicate that soot oxidation occurs simultaneously via two different mechanisms: one involving chemisorbed oxygen and/or lattice oxygen from the surface and the other involving lattice-bulk oxygen, with both pathways likely having a similar quantitative influence.

Supplementary Materials: The following supporting information can be downloaded at: https://www.mdpi.com/article/10.3390/molecules30020343/s1. Table S1. Surface elemental composition and atomic valence state determined via XPS; Table S2. Hydrogen consumption during TPR measurements. Figure S1. XRD diffractogram for the studied catalysts. Figure S2. Three independent activity measurements of the 0.25Mn-0.75Ce catalyst.

Author Contributions: Conceptualization, M.R.; methodology, M.R.; validation, M.R.; formal analysis, M.R.; investigation, M.R. and K.K.-W.; data curation, M.R.; writing—original draft preparation, M.R.; writing—review and editing, M.R. and K.K.-W.; visualization, M.R. All authors have read and agreed to the published version of the manuscript.

Funding: This research received no external funding.

Institutional Review Board Statement: Not applicable.

Informed Consent Statement: Not applicable.

Data Availability Statement: Data are contained within the Article and Supplementary Materials.

Conflicts of Interest: The authors declare no conflicts of interest.

References

1. Zhang, Z.; Dong, R.; Lan, G.; Yuan, T.; Tan, D. Diesel particulate filter regeneration mechanism of modern automobile engines and methods of reducing PM emissions: A review. *Environ. Sci. Pollut. Res.* **2023**, *30*, 39338–39376. [CrossRef]
2. Luo, J.; Zhang, H.; Liu, Z.; Zhang, Z.; Pan, Y.; Liang, X.; Wu, S.; Xu, H.; Xu, S.; Jiang, C. A review of regeneration mechanism and methods for reducing soot emissions from diesel particulate filter in diesel engine. *Environ. Sci. Pollut. Res.* **2023**, *30*, 86556–86597. [CrossRef] [PubMed]
3. Wu, Q.; Jing, M.; Wei, Y.; Zhao, Z.; Zhang, X.; Xiong, J.; Liu, J.; Song, W.; Li, J. High-efficient catalysts of core-shell structured Pt@transition metal oxides (TMOs) supported on 3DOM-Al_2O_3 for soot oxidation: The effect of strong Pt-TMO interaction. *Appl. Catal. B-Environ.* **2019**, *244*, 628–640. [CrossRef]
4. Liu, S.; Luo, S.; Wu, H.; Wang, T.; Ran, R.; Weng, D.; Si, Z.; Liu, S. Application of silica-alumina as hydrothermally stable supports for Pt catalysts for acid-assisted soot oxidation. *Rare Met.* **2023**, *42*, 1614–1623. [CrossRef]
5. Liu, S.; Wu, X.; Weng, D.; Li, M.; Ran, R. Roles of acid sites on Pt/H-ZSM5 catalyst in catalytic oxidation of diesel soot. *ACS Catal.* **2015**, *5*, 909–919. [CrossRef]
6. Wei, J.; Fan, C.; Zhuang, Y.; Fu, Z.; Guan, Z.; Li, H.; Li, D.; Qian, Y. Diesel soot combustion over ceria catalyst: Evolution of functional groups on soot surfaces. *Fuel* **2023**, *338*, 127391. [CrossRef]
7. Huang, J.; Wang, S.; Wang, X.; Gao, J.; Wang, Y.; Tian, G. Study on the differences between non-catalytic and catalytic oxidation of soot based on catalyst CeO_2. *J. Energy Inst.* **2024**, *113*, 101506. [CrossRef]

8. Bensaid, S.; Russo, N.; Fino, D. CeO_2 catalysts with fibrous morphology for soot oxidation: The importance of the soot-catalyst contact conditions. *Catal. Today* **2013**, *216*, 57–63. [CrossRef]
9. Machida, M.; Murata, Y.; Kishikawa, K.; Zhang, D.; Ikeue, K. On the reasons for high activity of CeO_2 catalyst for soot oxidation. *Chem. Mater.* **2008**, *20*, 4489–4494. [CrossRef]
10. Zouaoui, N.; Issa, M.; Kehrli, D.; Jeguirim, M. CeO_2 catalytic activity for soot oxidation under NO/O_2 in loose and tight contact. *Catal. Today* **2012**, *189*, 65–69. [CrossRef]
11. Krishna, K.; Bueno- López, A.; Makkee, M.; Moulijn, J.A. Potential rare earth modified CeO_2 catalysts for soot oxidation: I. Characterization and catalytic activity with O_2. *Appl. Catal. B-Environ.* **2007**, *75*, 189–200. [CrossRef]
12. Lee, J.H.; Kim, M.J.; Lee, E.J.; Lee, D.-W.; Kim, C.H.; Lee, K.-Y. Promoting effect of Rh-impregnation on Ag/CeO_2 catalyst for soot oxidation. *Appl. Surf. Sci.* **2022**, *572*, 151504. [CrossRef]
13. Gross, M.S.; Ulla, M.A.; Querini, C.A. Catalytic oxidation of diesel soot: New characterization and kinetic evidence related to the reaction mechanism on K/CeO_2 catalyst. *Appl. Catal. A-Gen.* **2009**, *360*, 81–88. [CrossRef]
14. Martínez-Munuera, J.C.; Cortés-Reyes, M.; García-García, A. An isotopic study on oxygen uptake/exchange over ceria-praseodymia mixed oxides with pulse experiments using $^{18}O_2$: Implications on soot combustion activities in the GDI (Gasoline Direct Injection) context. *Appl. Catal. B-Environ.* **2023**, *329*, 122525. [CrossRef]
15. Yamazaki, K.; Kayama, T.; Dong, F.; Shinjoh, H. A mechanistic study on soot oxidation over CeO_2-Ag catalyst with 'rice-ball' morphology. *J. Catal.* **2011**, *282*, 289–298. [CrossRef]
16. Medina, J.C.; Rodil, S.E.; Zanella, R. Synthesis of a CeO_2/Co_3O_4 catalyst with a remarkable performance for the soot oxidation reaction. *Catal. Sci. Technol.* **2020**, *10*, 853–863. [CrossRef]
17. Stegmayer, M.A.; Irusta, S.; Miró, E.E.; Milt, V.G.; Electrospinning synthesis and characterization of nanofibers of Co, Ce and mixed Co-Ce oxides. Their application to oxidation reactions of diesel soot and CO. *Catal. Today* **2022**, *383*, 266–276. [CrossRef]
18. Wang, H.; Jin, B.; Wang, H.; Ma, N.; Liu, W.; Weng, D.; Wu, X.; Liu, S. Study of Ag promoted Fe_2O_3@CeO_2 as superior soot oxidation catalysts: The role of Fe_2O_3 crystal plane and tandem oxygen delivery. *Appl. Catal. B-Environ.* **2018**, *237*, 251–262. [CrossRef]
19. Jampaiah, D.; Velisoju, V.K.; Devaiah, D.; Singh, M.; Mayes, E.L.H.; Coyle, V.E.; Reddy, B.M.; Bansal, V.; Bhargava, S.K. Flower-like Mn_3O_4/CeO_2 microspheres as an efficient catalyst for diesel soot and CO oxidation: Synergistic effects for enhanced catalytic performance. *Appl. Surf. Sci.* **2019**, *473*, 209–221. [CrossRef]
20. Rotko, M.; Karpińska-Wlizło, K.; Dubińska, N.; Gac, W. Soot oxidation on Mn_3O_4-CeO_2 catalysts. *Przem. Chem.* **2023**, *102*, 583–588.
21. Wagloehner, S.; Nitzer-Noski, M.; Kureti, S. Oxidation of soot on manganese oxide catalysts. *Chem. Eng. J.* **2015**, *259*, 492–504. [CrossRef]
22. Singer, C.; Kureti, S. Soot oxidation in diesel exhaust on manganese oxide catalyst prepared by flame spray pyrolysis. *Appl. Catal. B-Environ.* **2020**, *272*, 118961. [CrossRef]
23. Rotko, M.; Machocki, A. Evaluation of activity of catalytic materials used for soot oxidation in exhaust gases from Diesel engines. *Przem. Chem.* **2014**, *93*, 1846–1849.
24. Gao, Y.; Wang, Z.; Cui, C.; Wang, B.; Liu, W.; Liu, W.; Wang, L. Amorphous manganese oxide as highly active catalyst for soot oxidation. *Environ. Sci. Pollut. Res.* **2020**, *27*, 13488–13500. [CrossRef]
25. Atribak, I.; Bueno-López, A.; García-García, A.; Navarro, P.; Frías, D.; Montes, M. Catalytic activity for soot combustion of birnessite and cryptomelane. *Appl. Catal. B-Environ.* **2010**, *93*, 267–273. [CrossRef]
26. Wasalathanthri, N.D.; SantaMaria, T.M.; Kriz, D.A.; Dissanayakea, S.L.; Kuoa, C.-H.; Biswas, S.; Suiba, S.L. Mesoporous manganese oxides for NO_2 assisted catalytic soot oxidation. *Appl. Catal. B-Environ.* **2017**, *201*, 543–551. [CrossRef]
27. Kuwahara, Y.; Kato, G.; Fujibayashi, A.; Mori, K.; Yamashita, H. Diesel soot combustion over Mn_2O_3 catalysts with different morphologies: Elucidating the role of active oxygen species in soot combustion. *Chem. Asian. J.* **2020**, *15*, 2005–2014. [CrossRef] [PubMed]
28. Bueno-López, A.; Krishna, K.; Makkee, M.; Moulijn, J.A. Active oxygen from CeO_2 and its role in catalysed soot oxidation. *Catal. Lett.* **2005**, *99*, 203–205. [CrossRef]
29. Bueno-López, A. Diesel soot combustion ceria catalysts. *Appl. Catal. B-Environ.* **2014**, *146*, 1–11. [CrossRef]
30. Rotko, M. The use of $^{18}O_2$ to investigate the soot oxidation process on Co_3O_4, Co_3O_4-CeO_2 and CeO_2 catalysts in tight contact conditions. *Catal. Commun.* **2023**, *177*, 106644. [CrossRef]
31. Gross, M.S.; Ulla, M.A.; Querini, C.A. Diesel particulate matter combustion with CeO_2 as catalyst. Part I: System characterization and reaction mechanism. *J. Mol. Catal. A-Chem.* **2012**, *352*, 86–94. [CrossRef]
32. Mao, X.; Liu, S.; Liu, W.; Wu, X.; Liu, S. A simple model catalyst study to distinguish the roles of different oxygen species in propane and soot combustion. *Appl. Catal. B-Environ.* **2022**, *310*, 121331. [CrossRef]
33. Shannon, S.L.; Goodwin, J.G., Jr. Characterization of catalytic surfaces by isotopic-transient kinetics during steady-state reaction. *Chem. Rev.* **1995**, *95*, 677–695. [CrossRef]

34. Ledesma, C.; Yang, J.; Chen, D.; Holmen, A. Recent approaches in mechanistic and kinetic studies of catalytic reactions using SSITKA technique. *ACS Catal.* **2014**, *4*, 4527–4547. [CrossRef]
35. Jabłońska, M. An application of steady-state isotopic-transient kinetic analysis (SSITKA) in DeNOx process. *ChemCatChem.* **2021**, *13*, 818–827. [CrossRef]
36. Holmen, A.; Yang, J.; Chen, D. Steady-state isotopic transient kinetic analysis (SSITKA). In *Springer Handbook of Advanced Catalyst Characterization*; Wachs, I.E., Bañares, M.A., Eds.; Springer: New York, NY, USA, 2023.
37. Rotko, M.; Zawadzki, W.; Redko, V. Steady state isotopic transient kinetic analysis of the combustion of CH_4 over Co-Mn-O catalysts. *Catal. Commun.* **2019**, *125*, 32–36. [CrossRef]
38. Yang, Z.; Luo, L.; Tang, L.; Zhou, Z.; Zhou, Z.; Li, Y. Trimesic acid assisted synthesis of cerium-manganese oxide for catalytic diesel soot elimination: Enhancement of thermal aging resistibility. *Fuel* **2020**, *278*, 118369. [CrossRef]
39. Lin, X.; Li, S.; He, H.; Wu, Z.; Wu, J.; Chen, L.; Ye, D. Evolution of oxygen vacancies in MnO_x-CeO_2 mixed oxides for soot oxidation. *Appl. Catal. B-Environ.* **2018**, *223*, 91–102. [CrossRef]
40. Sacco, N.A.; Bortolozzi, J.P.; Milt, V.G.; Miró, E.E.; Banús, E.D. One step citric acid-assisted synthesis of Mn-Ce mixed oxides and their application to diesel soot combustion. *Fuel* **2022**, *322*, 124201. [CrossRef]
41. Huang, H.; Liu, J.; Sun, P.; Ye, S.; Liu, B. Effects of Mn-doped ceria oxygen-storage material on oxidation activity of diesel soot. *RSC Adv.* **2017**, *7*, 7406–7412. [CrossRef]
42. Wang, J.; Yang, S.; Sun, H.; Qiu, J.; Men, Y. Highly improved soot combustion performance over synergetic $Mn_xCe_{1-x}O_2$ solid solutions within mesoporous nanosheets. *J. Colloid Interf. Sci.* **2020**, *577*, 355–367. [CrossRef]
43. Zhu, M.; Wen, Y.; Shi, L.; Tan, Z.; Shen, Y.; Yin, K.; Sun, L. Revealing the promoting effect of multiple Mn valences on the catalytic activity of CeO_2 nanorods toward soot oxidation. *Nanoscale* **2022**, *14*, 11963–11971. [CrossRef] [PubMed]
44. Sacco, N.A.; Miró, E.E.; Milt, V.G.; Banús, E.D.; Bortolozzi, J.P. Kinetic, stability and characterization studies of Ce, Mn and Mn-doped ceria paper catalysts towards soot combustion under different reaction conditions. *Top. Catal.* **2022**, *65*, 1262–1272. [CrossRef]
45. Liu, Y.; Li, S.; Liu, X.; Tang, J.; Quan, W.; Cheng, H.; Chen, Z.; Wei, X.; Zhuang, J. Enhanced catalytic oxidation of toluene over heterostructured CeO_2-CuO-Mn_3O_4 hollow nanocomposites. *Colloids Surf. A Physicochem. Eng. Asp.* **2023**, *658*, 130671. [CrossRef]
46. Soldatova, A.V.; Balakrishnan, G.; Oyerinde, Q.F.; Romano, C.A.; Tebo, B.M.; Spiro, T.G. Biogenic and synthetic MnO_2 nanoparticles: Size and growth probed with absorption and Raman spectroscopies and dynamic light scattering. *Environ. Sci. Technol.* **2019**, *53*, 4185–4197. [CrossRef]
47. Thareja, S.; Kumar, A. One-pot in situ synthesis of Mn_3O_4/N-rGO nanohybrids for the fabrication of high cell voltage aqueous symmetric supercapacitors: An analysis of redox activity of Mn_3O_4 toward stabilizing the high potential window in salt-in-water and water-in-salt electrolytes. *Energy Fuels* **2022**, *36*, 15177–15187.
48. Feng, N.; Zhu, Z.; Zhao, P.; Wang, L.; Wan, H.; Guan, G. Facile fabrication of trepang-like CeO_2@MnO_2 nanocomposite with high catalytic activity for soot removal. *Appl. Surf. Sci.* **2020**, *515*, 146013. [CrossRef]
49. Tang, Q.; Du, J.; Xie, B.; Yang, Y.; Yu, W.; Tao, C. Rare earth metal modified three dimensionally ordered macroporous MnO_x-CeO_2 catalyst for diesel soot combustion. *J. Rare Earths* **2018**, *36*, 64–71. [CrossRef]
50. Colman-Lerner, E.; Peluso, A.M.; Sambeth, J.; Thomas, H. Cerium, manganese and cerium/manganese ceramic monolithic catalysts. Study of VOCs and PM removal. *J. Rare Earths* **2016**, *34*, 675–682. [CrossRef]
51. Jin, B.; Wu, X.; Weng, D.; Liu, S.; Yu, T.; Zhao, Z.; Wei, Y. Roles of cobalt and cerium species in three-dimensionally ordered macroporous $Co_xCe_{1-x}O_\delta$ catalysts for the catalytic oxidation of diesel soot. *J. Colloid Interface Sci.* **2018**, *532*, 579–587. [CrossRef] [PubMed]
52. Piumetti, M.; Fino, D.; Russo, N. Mesoporous manganese oxides prepared by solution combustion synthesis as catalysts for the total oxidation of VOCs. *Appl. Catal. B* **2015**, *163*, 277–287. [CrossRef]

Disclaimer/Publisher's Note: The statements, opinions and data contained in all publications are solely those of the individual author(s) and contributor(s) and not of MDPI and/or the editor(s). MDPI and/or the editor(s) disclaim responsibility for any injury to people or property resulting from any ideas, methods, instructions or products referred to in the content.